JACS
JOURNAL OF THE AMERICAN CHEMICAL SOCIETY

Article

pubs.acs.org/JACS

# Comprehensive Insights into the Structural and Chemical Changes in Mixed-Anion FeOF Electrodes by Using Operando PDF and NMR Spectroscopy

Kamila M. Wiaderek,[†] Olaf J. Borkiewicz,[†] Elizabeth Castillo-Martínez,[‡,§] Rosa Robert,[‡,⊥,#] Nathalie Pereira,[∥] Glenn G. Amatucci,[∥] Clare P. Grey,[‡,⊥] Peter J. Chupas,[†] and Karena W. Chapman*[,†]

[†]X-ray Science Division, Advanced Photon Source, Argonne National Laboratory, Argonne, Illinois 60439, United States

[‡]Department of Chemistry, University of Cambridge, Lensfield Road, Cambridge CB2 1EW, United Kingdom

[§]CIC Energigune, Albert Einstein 48, 01510 Miñano (Álava), Spain

[⊥]Department of Chemistry, Stony Brook University, Stony Brook, New York 11794-3400, United States

[∥]Energy Storage Research Group, Department of Materials Science and Engineering, Rutgers University, North Brunswick, New Jersey 08902, United States

Supporting Information

**ABSTRACT:** In-depth analysis of operando X-ray pair distribution function (PDF) data is combined with Li NMR spectroscopy to gain comprehensive insights into the electrochemical reaction mechanism of high-performance iron oxyfluoride electrodes. While the full discharge capacity could be recovered upon charge, implying reversibility of the electrochemical reaction, the atomic structure of the electrode formed after cycling (discharge−charge) differs from the pristine uncycled electrode material. Instead, the "active" electrode that forms upon cycling is a nanocomposite of an amorphous rutile phase and a nanoscale rock salt phase. Bond valence sum analysis, based on the precise structural parameters (bond lengths and coordination number) extracted from the in situ PDF data, suggests that anion partitioning occurs during the electrochemical reaction, with the rutile phase being F-rich and the rock salt phase being O-rich. The F- and O-rich phases react sequentially; Fe in a F-rich environment reacts preferentially during both discharge and charge.

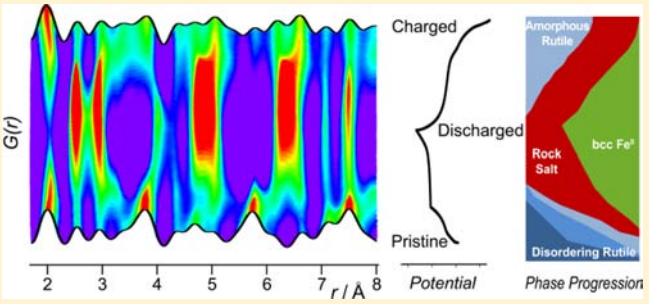


## INTRODUCTION

In the search for new Li-ion battery electrodes that provide the best compromise between capacity, power, charge rates, and long-term stability, increasingly complex composite materials and reaction mechanisms have emerged.[1] Among these materials, the high-capacity conversion electrodes based on highly abundant iron and mixed-anion oxyfluoride systems[2] combine favorable performance characteristics of the simple oxides (e.g., $Fe_2O_3$, $Fe_3O_4$, FeO)[3] and fluorides (e.g., $FeF_3$, $FeF_2$).[4] The electrochemical reaction of the oxyfluoride with lithium ($FeOF + 3Li \rightarrow Fe + Li_2O + LiF$, 884 mAh $g^{-1}$) couples the higher output voltages and reaction potentials of the fluorides and the improved reaction kinetics, capacity and cyclability of the oxides to provide promising electrochemical performance. Identifying the fundamental basis for these performance advantages requires a comprehensive understanding of the electrochemical reaction mechanism and, accordingly, detailed knowledge of how the atomic structure transforms, how the electrode particles evolve, and how the chemical compositions of different components change.

Iron oxyfluoride, a structural analogue of iron(II) fluoride ($FeF_2$), crystallizes with a rutile structure (tetragonal, $P4_2/mnm$, $a \approx 4.68$ Å, $c \approx 3.0$−$3.3$ Å) featuring corner-sharing and edge-sharing Fe octahedra.[5] The O and F are not long-range ordered over the anion lattice sites, although some short-range ordering is evident in the stoichiometric phase.[6] A series of iron oxyfluorides of composition $Fe^{II}_{(1-x)}Fe^{III}_xO_xF_{2-x}$ ($x = 0$−$1$), can be prepared by varying the O:F ratio during synthesis.[2] The $c$ lattice dimension, theoretical capacity and the initial Fe oxidation state increase linearly with O content.

Not only does the mixed-anion chemistry increase the complexity of the electrode and the electrochemical reaction, it also amplifies the already significant challenge in understanding the reaction mechanism. The general characterization challenge for conversion-based electrodes arises from the disruption of long-range structural order, that is, amorphization and/or nanoparticle formation, that accompanies pronounced restructuring during cycling.[3] This limits the utility of standard

**Received:** January 8, 2013
**Published:** February 22, 2013





dx.doi.org/10.1021/ja400229v | J. Am. Chem. Soc. 2013, 135, 4070−4078

crystallographic tools for structure analysis. In addition to characterizing how the electrode phase, atomic structure, and particle morphology evolve during cycling, the environment and reaction pathways for the individual anions must be distinguished. Characterization tools sensitive to both the structure and chemistry of the electrode are needed.

Distinguishing oxygen and fluorine is a perpetual challenge, even for the structural probes that have yielded the most comprehensive understanding of electrochemical conversion reactions to date. Nuclear magnetic resonance (NMR) spectroscopy is an element specific probe that can provide insight into the local environment of Li, as it intercalates and reacts with the electrode, as well as separately probing the environments of O and F nuclei.[7,8] However, in many conversion systems, including Fe-based materials, extrusion of paramagnetic nanoparticles during the conversion limits application of this methodology in this regime, impeding O/F specific analysis. Pair distribution function (PDF) analysis of total scattering data can provide detailed insights into the local atomic structure, phase progression, and particle size/ordering in conversion electrodes, independent of long-range order.[9−12] However as a scattering methodology, where element discrimination relies on scattering contrast, the near identical scattering power of O and F, for both X-rays and neutrons, prevents direct differentiation of these species in the PDF analysis.[13]

The PDF provides atomic-scale structural insights as a histogram of the atom−atom distances within the material, from the local coordination geometry extending to several nanometers: peaks within the PDF correspond directly to bond lengths and atom−atom distances within the material; the spatial extent of well-defined peaks in the PDF correspond the length scale over which the structure is ordered (i.e., particle size or local structural units within an amorphous system). The intensities of peaks within the PDF are related to the relative abundance of each atom−atom distance, that is the coordination number and relative abundance of a particular species or component. Materials insights can be extracted directly from the PDF, independent of a structure model, by considering the position (i.e., bond length) and intensity/area (i.e., coordination numbers/phase abundance) of selected peaks within the PDF (quantified through fitting of Gaussian functions). Alternatively, the entire PDF can be fit with crystallographic structure models, in a real-space analogue to Rietveld refinement of diffraction data, to identify phases, phase fractions in multicomponent systems, and approximate stoichiometries. This is possible for crystalline, nanocrystalline and amorphous materials alike (whereas diffraction analysis is only applicable to crystalline materials). The length scale of ordering within amorphous systems or the particle size in nanocrystalline materials can be refined as part of this model.

The intensity of features in the PDF are weighted by scattering amplitude of the atoms in each pair, and so PDFs derived from X-ray scattering data are most sensitive to components containing the higher $Z$ (i.e., strongly scattering) Fe atoms. The contribution from Li species (e.g., as ions intercalated within the electrode or as salts) is relatively insignificant,[14] requiring application of alternative probes (e.g., neutron PDF) or complementary methods such as $^6$Li NMR spectroscopy. While $^7$Li is a more abundant nucleus (93% natural abundance; $I$ = 3/2), it is more strongly affected by homonuclear dipolar coupling and interactions with the paramagnetic ions, both potentially leading to a broadening of the NMR signal. Narrower signals, with fewer spinning sidebands, can be obtained for $^6$Li NMR (7% natural abundance; $I$ = 3/2), although isotopic enrichment is generally required to obtain spectra with adequate signal-to-noise. Note, however, that even the $^6$Li NMR spectra of paramagnetic materials such as the iron oxides, fluorides, oxyfluorides studied here will suffer additional broadening due to large nuclear-unpaired electron interactions, as compared to the $^6$Li spectra of diamagnetic materials.

Here we combine an in-depth analysis of operando X-ray PDF data with $^6$Li NMR spectroscopy to gain comprehensive insights into the electrochemical reaction mechanism of high-performance iron oxyfluoride electrodes. The in situ nature of the PDF measurements—the first of their kind—is particularly revolutionary, providing exceptionally precise structural parameters from which new element specific insights, separating the evolution of O and F species, can be deduced. These element specific insight were recovered from an analysis of the bond valence sum utilizing the bond lengths and coordination numbers extracted from the PDFs. Iron oxyfluorides prepared with different O:F ratios ($Fe^{II}_{(1-x)}Fe^{III}_xO_xF_{2-x}$ for varying values of $x \approx 0.49-0.64$) were compared. The precise data available at fine reaction intervals (every 0.05Li reacted or ∼72 points over discharge−charge cycle in the present study), allowed reliable analysis of complex multiphase behaviors and transient intermediates to be captured. Complex behaviors documented during cycling include a multistep sequence of structural transitions, partitioning of the oxo- and fluoro anions, and formation of amorphous and nanoparticle phases. $^6$Li NMR spectroscopy yielded insight into the local environment of the Li ions at the beginning of the discharge and at the end charge processes. The coexistence of Li in diamagnetic (e.g., solid electrolyte interphase, SEI) and paramagnetic (oxidized Fe phase) environments can be readily deduced. Formation of superparamagnetic (Fe) nanoparticles at deeper discharge is evident via the attenuation of the $^6$Li NMR signal.

Intriguingly, while discharge capacity can be completely recovered upon charge—which is often taken to imply reversibility of an electrochemical reaction—the atomic structure and $^6$Li chemical shift of electrode formed after cycling (discharge−charge) differs from the pristine rutile phase originally enclosed in the electrochemical cell. This "active" electrode phase formed after (repeated) cycling is important in understanding the reversibility of the electrochemical cycling and the long-term electrode stability.

## EXPERIMENTAL METHODS

**Synthesis of $Fe^{II}_{(1-x)}Fe^{III}_xO_xF_{2-x}$.** Iron oxyfluoride samples ($Fe^{II}_{(1-x)}Fe^{III}_xO_xF_{2-x}$, $x$ = 0.49−0.64) were prepared via a solution process from Fe metal and aqueous fluorosilicic acid as described previously.[2] The C/FeOF nanocomposite was prepared by high-energy mechanomilling with 15 wt % carbon. Samples from three separate syntheses were used for the electrochemistry studies. The sample compositions, estimated to be $x \approx 0.64$ (NMR), $x \approx 0.60$ (in situ PDF), and $x \approx 0.49$ (in situ PDF and NMR) based on the lattice dimensions determined by refinement of a rutile model against the PDF of the as-synthesized nanocomposites (see Supporting Information (SI)).

**Synthesis of Model Compounds for NMR Studies.** $^6$Li-enriched rock-salt-type $\alpha$-$LiFeO_2$ and trirutile-type $LiFe_2F_6$ model compounds were prepared by solid-state synthesis. Rock-salt-type $\alpha$-$LiFeO_2$ was produced by grinding 20% excess of $^6Li_2CO_3$ (Sigma, 95% enriched, 99.9% purity) with $\alpha$-$Fe_2O_3$ and heating at 900 °C for 12 h.[15] A modified process based on that described in ref 16 was used to


dx.doi.org/10.1021/ja400229v | J. Am. Chem. Soc. 2013, 135, 4070−4078

synthesize $LiFe_2F_6$. A 20% excess of $^6LiF$ was mixed with stoichiometric ratios of $FeF_3$ and $FeF_2$ and milled for 1 h in a high-energy ball mill (Spex 8000) using a zirconia jar with two zirconia balls. The milled powder was pressed into a pellet, placed in an alumina crucible, and heated for 12 h at 500 °C, all under an Ar atmosphere.

**PDF Analysis.** For in situ PDF measurements, electrode pellets of the C/FeOF nanocomposite for $x = 0.49$ and 0.60 were prepared. The C/FeOF (12−15 mg) was mixed with carbon ("super P", Alfa Aesar), carbon black, and PTFE binder (Sigma-Aldrich) in the mass ratio 6:1:1:2 and formed into pellets (10 mm diameter, 120−180 $\mu$m thick).

The electrode pellets were assembled into an electrochemical cell suitable for in situ measurements (the "AMPIX" electrochemical cell)[17] with a glass fiber separator (Whatman GF/A), Li metal foil and liquid electrolyte (1 M $LiPF_6$ in 3:7 v:v ethylene carbonate:dimethylcarbonate (EC:DMC) from Tomiyama Pure Chemical Industries) within an Ar atmosphere glovebox. Cells were cycled galvanostatically against lithium at constant current of 30 mA/g (C/30), in the range 4.5−1.0 V for $x = 0.60$ at room temperature, and in the range 4.5−1.5 V for $x = 0.49$ and 0.60 at 50 °C. X-ray total scattering data suitable for PDF analysis were collected using 3 min exposures at 30 min intervals. Data were collected during the first discharge−charge cycle. The cycling rates and number of discharge−charge cycles studied was ultimately limited by the allocated beamtime.

X-ray scattering data were collected at the dedicated PDF beamline 11-ID-B at the Advanced Photon Source, Argonne National Laboratory. High-energy X-rays (~58 keV, $\lambda = 0.2128$ Å) were used in combination with a large amorphous-silicon based area detector (Perkin-Elmer) to collect total scattering data to high values of momentum transfer ($Q_{max} \approx 18$ Å).[18] The scattering images were reduced to one-dimensional data using fit2d.[19] These powder diffraction data show that the Bragg peaks are essentially eliminated after the initial stages of discharge and do not return (see SI). The data were corrected for background scattering, Compton scattering and detector effects within pdfgetX2 and Fourier transformed to get $G(r)$, the PDF.[20] The intensity and position of peaks corresponding to the Fe−O/F bond (~2.0 Å) and the Fe−Fe bond in metallic Fe (~2.5 Å) were quantified by fitting Gaussian functions within fityk.[21] Structure models were refined against the PDF data within PDFgui.[22] A spherical particle envelope was used to model the particle size and/or length scale of ordering. For data collected at elevated temperature, reduced ordering of the material and additional features, likely associated with electrolyte decomposition, complicated the analysis.

**NMR Analysis.** For NMR studies, electrodes were prepared by mixing the C/FeOF nanocomposite with additional carbon (10 wt %) and ball milling (1 h, Spex 8000 high-energy ball mill, zirconia jar with two zirconia balls). The resulting loose powders were used as cathodes without adding binder so as to obtain cleaner ($^{19}F$) NMR spectra. Cathode powder (5−10 mg) was assembled into coin cells (CR2032) with a glass fiber separator, 95%-enriched $^6Li$ metal foil (Sigma Aldrich) and liquid electrolyte (EC:DMC, 1:1 v:v; Novolyte) within an Ar atmosphere glovebox. Cells were galvanostatically cycled at rates of 8.8 mA/g and 18 mA/g (C/100 and C/50, respectively) and stopped at different states of discharge and charge. To perform $^6Li$ NMR spectroscopy, batteries were disassembled, and the cycled electrodes were washed twice with DMC so as to remove the maximum amount of $LiPF_6$ and EC. After vacuum drying, samples were packed into 1.8 mm zirconia rotors and closed with Vespel caps inside the glovebox. Note that these samples were unpacked in air following the $^6Li$ measurements and then later repacked into rotors for the $^{19}F$ measurements, again in air.

$^6Li$ and $^{19}F$ solid state NMR data were collected on a Bruker 200 MHz spectrometer, at an operating frequency of 29 and 188 MHz for $^6Li$ and $^{19}F$, respectively, with a 1.8 mm probe built by Ago Samoson. Rotors were spun at a magic-angle-spinning (MAS) rate of 39 kHz. A rotor synchronized Hahn echo (90°-$\tau$-180°-$\tau$-acq.) sequence was used with a 90° pulse of 2.75 $\mu$s ($^6Li$ and $^{19}F$) and delays of 0.1 s for $^6Li$ and 1.0 s for $^{19}F$. Approximately 360 000 scans were collected per $^6Li$ NMR spectrum. $^6Li$ spectra are referenced to 1 M $^6LiCl$ aqueous solution. Approximately 100 000 scans were collected per $^{19}F$ spectrum, the spectra being referenced to a secondary reference, solid LiF (−201 ppm).[23] The spectra shown in the plots are normalized with respect to the sample weight and number of scans.

## RESULTS

The electrochemical discharge−charge curves obtained during the in situ PDF measurements are shown in Figure 1. The

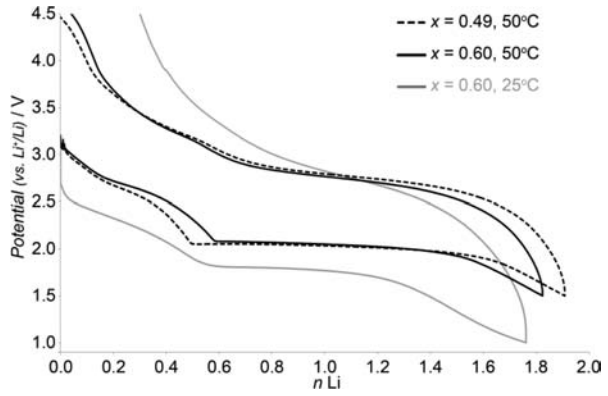


**Figure 1.** Discharge−charge curves obtained for $Fe^{II}_{(1-x)}Fe^{III}_xO_xF_{2-x}$ within the AMPIX cell during PDF measurements, with a cycling current of 30 mA/g.

potential drops initially on lithiation (Fe reduction), consistent with a solid solution mechanism, or a series of continually varying structures/compositions, both suggesting an intercalation process. It then attains a flat (subtly sloping) profile consistent with a process that resembles a two-phase reaction, as is generally observed for a straightforward conversion reaction. Finally, a sloping profile is seen, which is consistent with the insertion of lithium into an electrode with a continuing variation of sample composition/structure. For the electrode with higher oxygen content, a larger intercalation component and lower overall capacity were evident in this voltage window: for $x = 0.60$, the potential drops progressively with reaction of ~0.6Li, plateaus at ~2.08−1.95 V between 0.6 and 1.5Li, and starts to drop again reaching a potential of 1.5 V at 1.82Li. For $x = 0.49$, the potential drops progressively with reaction of ~0.5Li, plateaus at ~2.08−1.95 V between 0.6 and 1.6Li, and starts to drop again reaching a potential of 1.5 V at 1.92Li.

For the cell cycled at room temperature, the potentials were offset to lower potential (1.8 cf. 2.08 V), with a less well-defined transition between the intercalation and conversion regimes. This reflects the nonequilibrium conditions, and a distribution of sample charge/discharge states may then exist when cycling under these conditions. A galvanostatic intermittent titration study suggests that the potential may be offset to lower values by 0.4−0.7 V for cycling at room temperature, compared to the equilibrium conditions (see SI). The capacity is not fully recovered upon charging (delithiation/Fe oxidation). At elevated temperature (50 °C) the reaction kinetics are accelerated such that at cycling rates of 30 mA/g, equilibrium is attained and the full capacity is recovered upon charge.

The PDFs obtained during electrochemical cycling contain generally similar features and trends indicating that the mechanism is independent of cycling temperature and composition (Figure 2). Structural transitions observed with charge and discharge, seem largely reversible. The discharge product, presumably metallic Fe nanoparticles, is characterized by a short Fe−Fe contact of 2.5 Å. An intermediate, observed


dx.doi.org/10.1021/ja400229v | J. Am. Chem. Soc. 2013, 135, 4070−4078

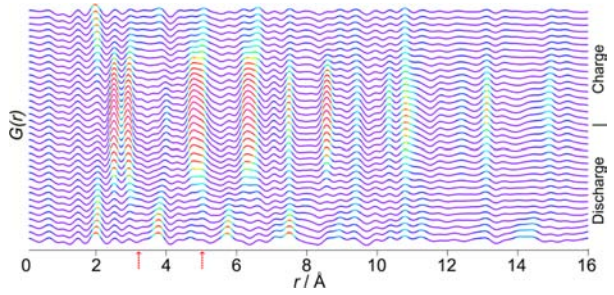


**Figure 2.** Selected PDFs obtained during the first discharge−charge cycle (for $x$ = 0.60, 50 °C, C/30, ∼35 h, 4.5−1.5−4.5 V) by Fourier transforming the total scattering X-ray data. The arrows indicate distances characteristic of the rock salt intermediate. The colors reflect relative peak intensities.

both during charge and discharge, is characterized by peaks at ∼3.2 and 5.0 Å which are not found in the pristine or discharged (to 1.5 or 1 V) states. The product at the end of charge contains features at low $r$, below ∼5 Å, similar to those of the pristine electrode. However, the features at longer distances are attenuated, suggesting a reduction in crystallinity and/or particle size.

The evolution of the phase fractions and particle sizes during cycling and the structure of the intermediate were identified from refinement of structural models against the PDF data (Figures 3 and 4). This analysis shows that the pristine rutile

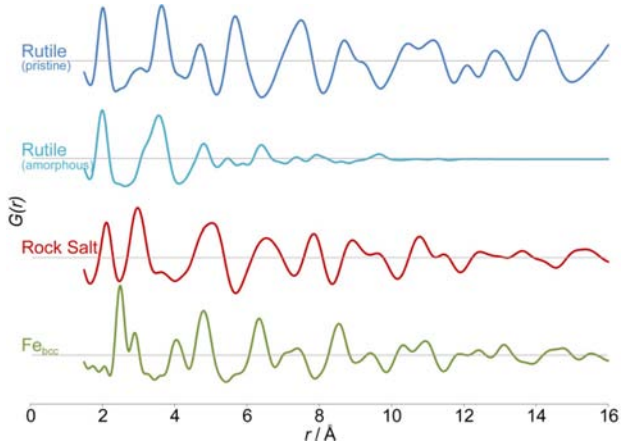


**Figure 3.** Simulated PDFs corresponding to the pristine rutile, rock salt, Fe nanoparticles, and amorphous rutile phase formed within the electrode during cycling.

phase becomes more disordered during the initial discharge, which was best modeled as change in relative populations of crystalline, distorted and amorphous rutile-type phases. This likely reflects heterogeneity within the electrode particles. There is no evidence for local O/F ordering in these nanoscale nonstoichiometric $FeO_xF_{2-x}$ phases.[6] Formation of an intermediate with a rock salt structure is evident from ∼0.4Li, before the plateau in the electrochemistry and/or the onset of iron nanoparticles formation. The rock salt intermediate has ordering of ∼50 Å at room temperature and ∼25 Å at 50 °C. Local structure distortions of this rock salt intermediate are similar to those in the $\alpha$-$LiFeO_2$ NMR model compound (see SI) and in the conversion reaction of $\alpha$-$Fe_2O_3$.[12] We propose that a similar intermediate forms here.

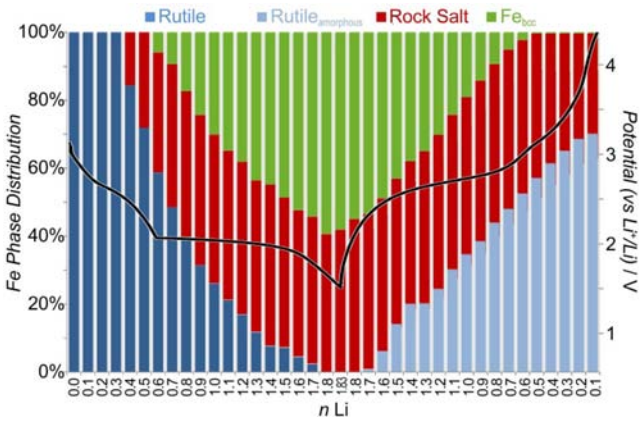


**Figure 4.** Evolution of Fe phases during cycling of $x$ = 0.60 at 50 °C from full profile fits to the PDF data. For simplicity, the increasingly disordered and amorphous character of the initial rutile electrode structure has been represented as a single component.

The body-centered cubic (bcc) Fe nanoparticles that form during discharge are ∼25 Å in diameter. Sharpening of the Fe peaks is evident in the early stages of charge, with continued ripening or growth of the Fe nanoparticles, even as Fe is being consumed by the charge processes (see Figure 2 and SI). This reflects the dynamic nature of the small metallic nanoparticles. Fits to the PDF data suggest that the nanoparticles grow to ∼30 Å (at 1.3−1.2Li) during charge.

Upon charge, the Fe nanoparticles are consumed as a poorly ordered rutile phase—referred to here as "amorphous rutile"—is formed. The amorphous rutile formed upon charge only shows ordered structural features below ∼6−10 Å, with an increased distortion, compared to crystalline rutile, of the corner- and edge-sharing connections between Fe polyhedra. While the limited range ordering could also be interpreted as discrete nanoparticles, nanoparticles of this size are typically highly reactive and would likely aggregate into large particles.

The rock salt phase does not react until late into charge, after all the Fe nanoparticles have transformed to amorphous rutile. Some rock salt remains in the fully charged material. For the electrode with higher oxygen content ($x$ = 0.60, cf, $x$ = 0.49), a greater fraction of the rock salt phase was evident in the charged electrode. The increase in rock salt component was directly proportional to the increase in oxygen anions (see SI).

The evolution of the peak positions and intensities were quantified by fitting Gaussian functions to selected peaks in the PDF (Figure 5). High precision in the PDF measurement and extraction provide for smooth trends in these features.

The first peak at ∼2.0 Å corresponds to the Fe−O and Fe−F correlation in the oxidized Fe phases (i.e., rutile and rock salt). The changes in peak position reflect changes in the average Fe−O and Fe−F bond length accompanying changes in Fe oxidation and the ratio of Fe−O to Fe−F bonds. Changes in the peak intensity reflect changes in the relative abundance of Fe−O/F bonds accompanying changes in the abundance of oxidized Fe phases or in the average Fe coordination number. The average Fe−X bond expands during the initial discharge, by about 0.05 Å at 0.5−0.6Li, beyond which it decreases slightly. This is consistent with the reduction of $Fe^{3+}$ to $Fe^{2+}$ during intercalation, followed by a likely change in the ratio Fe−O (shorter) to Fe−F (longer) bonds during conversion. The intensity of the Fe−X peak decreases monotonically with discharge. During the subsequent charge, there is pronounced


dx.doi.org/10.1021/ja400229v | J. Am. Chem. Soc. 2013, 135, 4070−4078

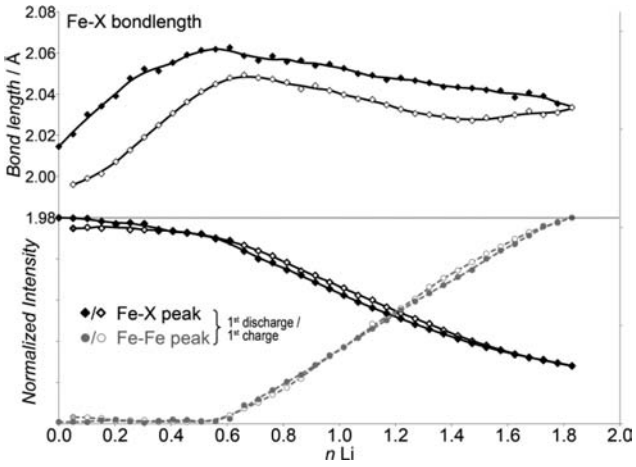


**Figure 5.** Selected peak positions and intensities corresponding to the Fe−X and Fe−Fe bonds for $x$ = 0.60 cycled at 50 °C.

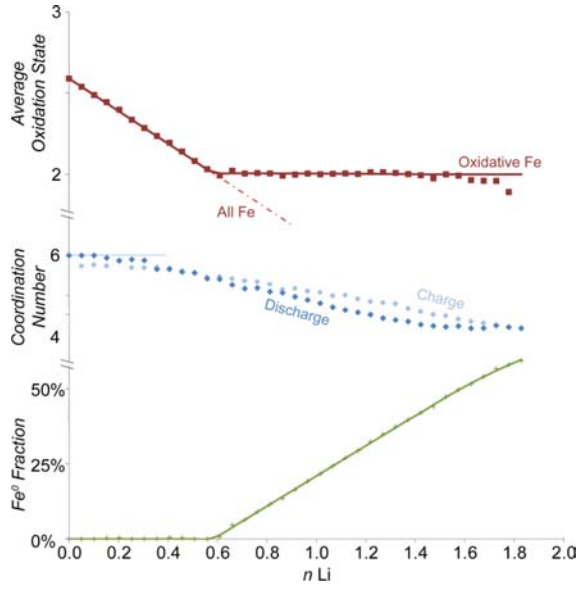


**Figure 6.** Average oxidation state and coordination number of Fe within the oxidized Fe phases, and the quantity of Fe extruded as $Fe^0$ during discharge for $x$ = 0.60 at 50 °C, based on the intensity of selected peaks within the PDFs.

hysteresis in the evolution of the Fe−X features. The turnover for the Fe−X peak position occurs at lower oxidation state (~0.7Li). The peak intensity plateaus earlier, at a lower maximum intensity.

The peak at 2.5 Å corresponds to the nearest-neighbor Fe−Fe distance in the bcc Fe metal. Not only does the appearance of this peak provides a clear indication of the onset of Fe metal formation, but it can also be used to quantify the abundance of $Fe^0$. For all cycling conditions, this peak started to grow during discharge at potentials of ~2.08 V, indicating Fe nanoparticle formation (and conversion) independent of whether a plateau is attained in the electrochemistry. The intensity of this peak corresponds to the relative abundance of Fe−Fe bonds. While this relates to both the abundance of $Fe^0$ and the nanoparticle size, given the relatively small variation in Fe nanoparticle size suggested by the phase analysis of the PDF data (during charge only ripening of the Fe nanoparticles from ~25 to 30 Å changes the average coordination number by <5%),[24] the peak intensity provides a good approximation to the relative $Fe^0$ concentration. This peak intensity can be normalized by the relative abundance of $Fe^0$ determined from a fit to the PDF data at a single point (e.g., at the end of discharge), such that the fraction of reduced Fe can be quantitatively determined throughout the cycling (see Figure 6). The evolution in the Fe−Fe peak intensity is consistent between discharge and charge.

The average Fe oxidation state in the oxidized Fe phases (i.e., rutile and rock salt) can be extrapolated from the initial oxidation state using the known quantity of Li reacted and $Fe^0$ formed.

$$\text{ox. state } (n\text{Li}) = [\text{ox. state } (0\text{Li}) - n\text{Li reacted}]/[1 - \text{Fe}^0 \text{ formed}]$$

This presumes that all Li is involved in the Fe reduction without side reactions, for example, to form an SEI.

The average oxidation state of the oxidized Fe, calculated in this way, is shown in Figure 6. The oxidation state decreases linearly from ~2.6 to 2, whereupon it plateaus. That the Fe oxidation state, calculated in this way, stabilizes at 2 during the plateau in the voltage profile, as is also seen in a Mossbauer analysis,[25] supports the reliability of this approach. This is in contrast with the behavior of $\alpha$-$Fe_2O_3$ in which disproportionation ($Fe^{2+} \rightarrow Fe^{3+} + Fe^0$) has been observed.[26] At high levels of lithiation, the projected Fe oxidation state falls below 2, which is unphysical and likely reflects reaction of Li with non-Fe species, for example, to form SEI. This occurs in the regime in which the electrochemical potential drops below ~2 V, where SEI formation has been observed.[27] This can be used to provide an indication of the onset of SEI formation.

The changes in the Fe coordination number can be determined from the change in the intensity of the Fe−X peak, renormalizing to account for the progressive conversion to $Fe^0$ (see Figure 6). The initial coordination number was assumed to be 6—the coordination number for Fe in rutile. The average Fe coordination number reduces from 6 and gradually plateaus at ~4.25, in the rock salt phase, toward the end of discharge. The lower coordination number in the rock salt phase may reflect defects within the structure (including the formation of tetrahedral and five-coordination sites) and/or the nanoscale nature of this phase, with its high surface-to-volume ratio.

While the X-ray data are insensitive to differences in the scattering contributions from O and F anions (indeed, the isoelectric $O^{2-}$ and $F^-$ have identical X-ray scattering amplitudes), the precise average bond length, coordination number and oxidation state information extracted from the in situ PDFs can provide quantitative insight into the O/F evolution based on the distinct distances characteristic of Fe−O and Fe−F bonds. Specifically, in a bond valence sum analysis, the weighting of Fe−O to Fe−F bond valence parameters[28] provides a measure of the ratio of Fe−F to Fe−O bonds throughout the reaction. While the empirical bond-valence parameters of Brese and O'Keeffe[28] used, provide relevant insights into the trends in compositions, nonequilibrium bond valence parameters[29] may yield more quantitative insights.

The relative ratio of Fe−O and Fe−F bonds was estimated by considering the weighting of Fe−O and Fe−F bond valence parameters suggested by the average Fe−O/F bond length, coordination number and oxidation state (see Figure 7). These reflect both changes to the chemistry of individual phases, as well as changes in the relative abundance of the oxidized Fe phases documented in the PDF phase analysis. The $Fe^{2+}/Fe^{3+}$


dx.doi.org/10.1021/ja400229v | J. Am. Chem. Soc. 2013, 135, 4070−4078

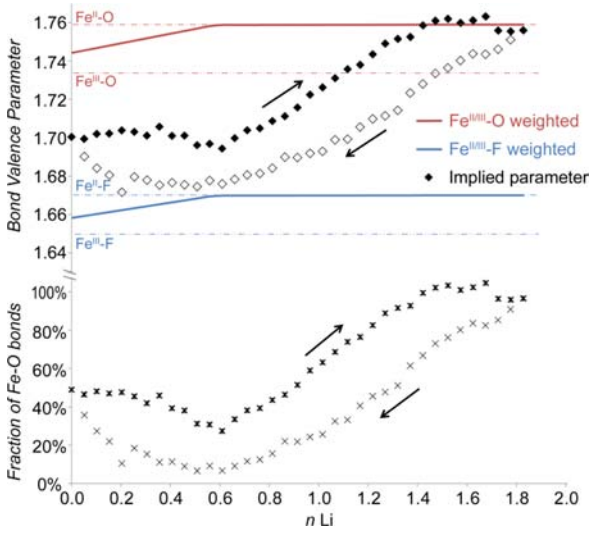


**Figure 7.** Average bond valence parameter implied by the average Fe oxidation state, coordination number and bond length in oxidized Fe phases, and the corresponding fraction of Fe−X bonds that are Fe−O. Arrows indicate the data obtained with discharge (lithiation, Fe reduction) and charge (delithiation, Fe oxidation).

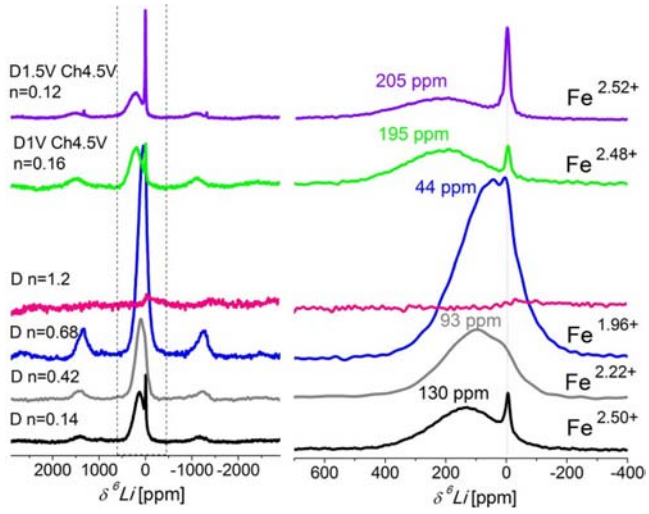


**Figure 8.** Normalized Hahn-echo $^6$Li MAS NMR spectra for $x$ = 0.64 $FeO_xF_{2-x}$ samples recovered from different states of discharge (D) and charge (Ch) following cycling at 8.8 mA/g at room temperature (a). The region showing the isotropic resonances has been expanded in (b). The most intense resonances are marked with their isotropic shifts.

parameters were weighted based on the average oxidation state. This analysis is more sensitive to variations in the Fe−O to Fe−F ratio, rather than changes in Fe oxidation state, with a factor of 4 larger difference in bond valence parameters for oxo and fluoro ligands. Systematic errors in the structural parameters may be associated with an offset of the estimated Fe−O/Fe−F bond ratio; however, given the consistency of the data provided by in situ measurements, these errors remain constant and the trends observed with cycling are unaffected.

The proportion of Fe−F bonds decreases approximately linearly between 0.6Li and 1.4Li, with exclusively Fe−O remaining in the oxidized Fe phases near the end of discharge. This suggests that the rock salt phase is primarily an oxide. During discharge F-coordinated Fe is preferentially reduced to form Fe nanoparticles and, presumably, LiF. This is consistent with the higher potentials typical of metal fluoride conversion reactions. The stabilization of the O:F ratio late in the discharge reaction (∼1.4−1.8Li), while $Fe^0$ continues to form, implies that some $Li_2O$ is formed here, although the PDF is not directly sensitive to these weakly scattering Li salts. The progressive change in O:F ratio in the oxidized Fe phase may underlie the slight slope in the voltage "plateau". It is possible that cycling over a more limited range, in which only F-coordinated Fe is reduced may further improve capacity retention.

Upon charge, the proportion of Fe−F bonds increases near linearly from the start of charge, during which the amorphous rutile phase is formed. This suggests that the amorphous rutile is fluoride-rich. Further this indicates that LiF reacts preferentially (as compared to $Li_2O$) during charge. The proportion of Fe−F increases to a maximum at ∼0.6Li beyond which the proportion of Fe−O increases and approaches the initial O:F ratio.

The $^6$Li NMR spectra early in discharge and late in charge (0.14−0.67Li) are dominated by two major resonances: a narrow signal at ∼0 ppm and a broad signal between 40 and 205 ppm (see Figure 8). The narrow peak corresponds to Li in a diamagnetic environment—likely residual electrolyte, SEI, LiF, and/or $Li_2O$ not removed by the sample washing. The broad signal is assigned to Li ions in close proximity to paramagnetic ($Fe^{2+/3+}$) ions, the shift arising from the Fermi contact interaction with the unpaired electrons.[30] At deeper discharge (∼1.2Li), no signal was detected. This presumably results from the strong dipolar interactions with the significant population of Fe superparamagnetic particles within the sample, which will broaden the NMR resonances so that they are no longer observed under the conditions used here.[9] (Signals with extremely large spinning sideband manifolds spanning ≫2000 ppm can be observed from the $^7$Li NMR spectra of samples with $n$ > 0.6; see SI.) The broad, shifted NMR $^6$Li signals observed early in the discharge are assigned to Li intercalated into the channels parallel to the chains of Fe(O/F) octahedra of the rutile structure. As $Li^+$ intercalation continues, and the Fe progressively reduces, the Fermi contact shift decreases, in a similar trend to that observed on $^6Li^+$ intercalation in $FeF_3$.[9] At the end of charge, the broad signal is likewise assigned to Li remaining in an environment close to paramagnetic $Fe^{2+}/Fe^{3+}$ ions. Importantly, despite the similar average oxidation state of the sample studied near the beginning of discharge and the end of charge, a significantly higher shift is evident upon charge (130 ppm cf. ∼200 ppm) suggesting that the $Li^+$ ions are in a different local environment and/or in nearby Fe ions with a higher average Fe oxidation state. The spectrum acquired on charge from a sample with a lower oxygen content ($x$ = 0.49) is similar, except that a slightly lower shift value of 186 ppm was observed (see SI), reflecting the higher residual Li content ($n$ = 0.2) and thus lower average Fe oxidation state. These shift values are also noticeably smaller than those observed for the model compounds $\alpha$-$LiFeO_2$, a disordered rock salt containing $Fe^{3+}$ only (530 ppm), the mixed $Fe^{2+}/Fe^{3+}$ trirutile phase $LiFe_2F_6$ (318 ppm) (Figure 9) and lithium-exchanged $\alpha$-$LiFeO_2$ (317 ppm).[31] Interestingly, the shift is slightly higher than that observed after cycling $FeF_3$ for one cycle (168 ppm).[9]

$^{19}$F NMR of the same materials show that some LiF is formed even at Li contents as low as 0.4 (see SI), which is ascribed to a combination of SEI formation and the instability of the lithiated Fe phase: over time, Fe extrusion and LiF formation occur.


dx.doi.org/10.1021/ja400229v | J. Am. Chem. Soc. 2013, 135, 4070−4078

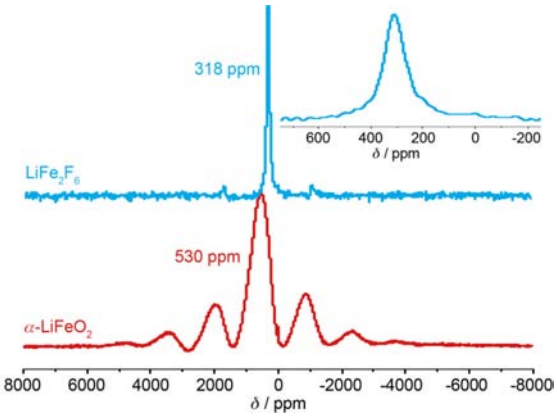


**Figure 9.** Normalized Hahn-echo $^6$Li MAS NMR spectra of $LiFe_2F_6$ and rock-salt-type $\alpha$-$LiFeO_2$.

## DISCUSSION

A fundamental question, central to developing an understanding of any conversion-based electrode material, relates to the nature of the "active" electrode—the electrode that exists after one or more discharge−charge cycles, that is, after reconversion. As conversion involves complete restructuring of the electrode, with cleavage of all original bonds, there is no prerequisite that the original material should be regenerated upon charge. This "active" electrode phase is key to understanding the reversibility of the electrochemical cycling, the long-term electrode stability, and, ultimately, to developing higher performance battery materials. While the recovery of the full discharge capacity upon charge, as observed here, is often taken to imply reversibility of the electrochemical reaction, and reformation of the original electrode the PDF and NMR analyses clearly indicate that the active electrode formed after cycling differs from the original rutile oxyfluoride phase enclosed in the electrochemical cell. While a change in the electrode particle size is expected, more pronounced chemical and structural differences are evident here. Notably, the electrode is no longer a single Fe phase but a two-phase mixture of rock salt and amorphous rutile. The variation in O/F coordination and phase composition from PDF analysis indicates that the amorphous rutile phase is fluoride-rich and that the rock salt phase is oxygen-rich. This anion partitioning is perhaps not unexpected given the metastability of oxyfluorides, many of which are known to decompose into pure oxides and fluorides upon heating,[2,32] and has been previously proposed to occur in conversion reactions of other oxyfluorides.[10] The partitioning is not necessarily quantitative; minority O anions in the reconverted rutile phase may frustrate ordering of the structure and contribute to its amorphous nature. Thermodynamic (e.g., variable-temperature) studies are needed to fully understand the amorphous nature of this phase.

While, the single-phase oxyfluoride was believed to enhance the electrochemical performance, combining the favorable characteristics of the pure oxide and fluorides, in reality, the active electrode that delivers the enhanced performance is actually a two-phase composite mixture of oxide-rich and fluoride-rich components. This suggests that synthesis of a single-phase mixed-anion (or mixed-cation) system is unnecessary and the similar performance enhancements in conversion systems may be realized cycling composite electrodes that are physical mixtures of oxides and fluorides. An appropriate nanostructuring of the composite may also be important. This may be a broadly applicable approach to enhance performance of high-capacity conversion electrodes.

The NMR data suggest that, following the first discharge, the residual $Li^+$ ions are proximal to a greater proportion of trivalent iron, a larger Fermi contact shift being evident in the electrode near the end of charge as compared to that observed early in the discharge (~200 ppm cf. 130 ppm), despite the similar *average* Fe oxidation state ($Fe^{\sim 2.6+}$). This larger hyperfine shift excludes the possibility that the residual Li is simply intercalated into the channels of a rutile structure. Further, there should be no impediment to complete delithiation of this intercalated Li under all cycling conditions. Note, however, that when Li is inserted into the rutile $FeO_xF_{2-x}$ structure, the $Li^+$ will be located in sites nearby $Fe^{2+}$ (not $Fe^{3+}$). In contrast, $Li^+$ ions that remain in the rutile or rock salt structures on charge, if they are located on the Fe sites, e.g., in either $Li_zFe_{1-z}F_2$ or $Li_{z'}Fe_{1-z'}O$, will be nearby more $Fe^{3+}$ ions (again for charge balance). Environments similar to that in model rock salt $\alpha$-$LiFeO_2$ ($Fe^{3+}$, 530 ppm) are plausible given the residual rock salt phase observed by PDF at the top of charge, but any residual rock salt phase must be associated with a lower Fe oxidation state than 3+. An environment directly comparable to that in model compound trirutile $LiFe_2F_6$, is excluded on the basis of its much larger hyperfine shift for a similar average oxidation state ($Fe^{2.5+}$, 318 ppm cf. $Fe^{2.6+}$, ~200 ppm). Thus, the NMR results appear to suggest that the residual Li is associated with a mixed $Fe^{2+}/Fe^{3+}$ rock salt phase, but some partial lithiated of the rutile structure cannot be completely excluded.

It is interesting to note that the F components react preferentially during both discharge and charge, such that the order of reaction mechanism with discharge and charge is not precisely reversed. While the F/O reaction sequence with discharge follows that expected based on the reaction potentials typical of the pure fluoride and oxide phases, the earlier reaction of LiF during reconversion is unexpected. This may reflect a greater mobility of $F^-$ anions, as well as a greater relative abundance (based in initial composition and the only partial conversion of the O-rich Fe phase). Residual $Li_2O$, if it reacts at this stage, must result in the formation of an oxyfluoride, not a rock salt.

A series of reactions may be written to describe the process. The first step involves the lithiation of the oxyfluoride and the gradual distortion of the rutile structure:

$$FeO_xF_{2-x} + n\mathrm{Li} \rightarrow Li_nFeO_xF_{2-x} \quad (n \leq x) \tag{1}$$

This phase is likely metastable, with evidence for the formation of LiF if this phase is left to relax (for example for the NMR experiments). This suggests reactions of the form

$$Li_nFeO_xF_{2-x} \rightarrow Li_{n-y}FeO_xF_{2-x-y} + y\mathrm{LiF} \tag{2a}$$

can occur, leading to a rock salt phase when $y$ approaches $2 - x$.

Alternatively, partitioning of the lithiated oxyfluoride may also contribute to the formation of the rock salt and amorphous rutile phase *before* Fe is observed in the in situ PDF experiments:

$$Li_nFeO_xF_{2-x} \rightarrow Li_{n-y}Fe_zO_x + Fe_{1-z}F_{2-x-y} + y\mathrm{LiF} \quad (x + y \leq z) \tag{2b}$$

The rock salt phase is also generated by further lithiation of $Li_nFeO_xF_{2-x}$, which can be written schematically as


dx.doi.org/10.1021/ja400229v | J. Am. Chem. Soc. 2013, 135, 4070−4078

$$Li_nFeO_xF_{2-x} + (2 - x - y)Li \rightarrow Li_{n-y}Fe_zO_x + (1 - y)Fe + (2 - x)LiF \quad (2c)$$

We assume the limit of reaction to form a largely fluorine-free rock salt phase.

Finally, the rock salt phase reacts further to form Fe and $Li_2O$ as the reaction potential decreases toward values more typical of iron oxides:[12]

$$Li_yFe_zO_x + (2x - y)Li \rightarrow zFe + xLi_2O \quad (3)$$

On charge, there is a steady conversion of the Fe (and presumably LiF) to initially to form rutile and not a rock salt phase. This is somewhat counterintuitive but is consistent with the potential, which is similar to that seen for $FeF_2$ on charge (see Figure S2). Experiments to investigate the reactions observed following discharge to lower voltages to form more $Li_2O$ are ongoing to determine if this influences the structural pathways taken on charge.

The reaction to form the rutile phase schematically involves an LiF:Fe interface and proceeds as follows:

$$Fe + yLiF \rightarrow FeF_y + yLi \quad (x \geq 2) \quad (4)$$

The formation of some partially lithiated rutile phases are also likely, as proposed by Doe et al. to occur on charging of $FeF_3$, particularly at higher states of charge.[33] Finally, some partial reaction of the rock salt and rutile phases occurs at the top of charge. The nonreversal of the O/F reaction sequence, likely contributes to the hysteresis in the reaction potential. In particular, reduction involves lithation (intercalation) and then phase segregation, while charging takes a different pathway with little or no intercalation, again resulting in hysteresis. DFT calculations are in progress to examine these processes.[34]

## CONCLUSION

In summary, we demonstrate that PDF analysis, applied in situ, during electrochemical cycling can provide detailed broad ranging insights into the chemical, structural and morphological transformations that occur during electrochemical conversion. Specifically, the precise structural parameters obtained for a single sample, without the potential sample variability or contamination that can occur with comparable ex situ studies, allowed reactions involving the oxide and fluoride anions to be separated. This revealed an unexpected preferential reaction of the fluoride component during both discharge and charge. This may contribute to the attractive electrochemical performance of this system. The characterization of the multiphase active electrode and how it is distinct from the single phase uncycled pristine material, has important implications in designing other mixed-anion systems. Competition between reactions involving the rock salt and rutile components in the active electrode, and frustration in O/F ordering within these phases, may all favor the nanosized composite electrode structure which contributes to enhanced cyclability.

## ASSOCIATED CONTENT

### Supporting Information

Details of sample preparation, PDF results, and NMR analysis. This material is available free of charge via the Internet at http://pubs.acs.org.

## AUTHOR INFORMATION


### Corresponding Author

chapmank@aps.anl.gov

### Present Address

[#]Paul Scherrer Institute, Switzerland


### Notes

The authors declare no competing financial interest.

## ACKNOWLEDGMENTS

This work was supported as part of NECCES, an Energy Frontier Research Center funded by the U.S. Department of Energy, Office of Science, Office of Basic Energy Sciences under award no. DE-SC0001294. Work done at Argonne and use of the Advanced Photon Source, an Office of Science User Facility operated for the U.S. Department of Energy Office of Science by Argonne National Laboratory, were supported by the U.S. Department of Energy under contract no. DE-AC02-06CH11357. The Generalitat de Catalunya is acknowledged for the postdoctoral research grant awarded to R.R. (BP-DGR 2008). We thank the members of the NECCES conversion thrust for many helpful discussions, and in particular G. Ceder and F. Cosandey.

## REFERENCES


(1) (a) Arico, A. S.; Bruce, P.; Scrosati, B.; Tarascon, J. M.; Van Schalkwijk, W. *Nat. Mater.* **2005**, *4*, 366. (b) Song, H. K.; Lee, K. T.; Kim, M. G.; Nazar, L. F.; Cho, J. *Adv. Funct. Mater.* **2010**, *20*, 3818. (c) Cabana, J.; Monconduit, L.; Larcher, D.; Palacin, M. R. *Adv. Mater.* **2010**, *22*, E170.

(2) Pereira, N.; Badway, F.; Wartelsky, M.; Gunn, S.; Amatucci, G. G. *J. Electrochem. Soc.* **2009**, *156*, A407.

(3) Poizot, P.; Laruelle, S.; Grugeon, S.; Dupont, L.; Tarascon, J. M. *Nature* **2000**, *407*, 496.

(4) Badway, F.; Pereira, N.; Cosandey, F.; Amatucci, G. G. *J. Electrochem. Soc.* **2003**, *150*, A1209.

(5) Vlasse, M.; Massies, J. C.; Demazeau, G. *J. Solid State Chem.* **1973**, *8*, 109.

(6) (a) Brink, F. J.; Withers, R. L.; Norén, L. *J. Solid State Chem.* **2001**, *161*, 31. (b) Brink, F. J.; Withers, R. L.; Thompson, J. G. *J. Solid State Chem.* **2000**, *155*, 359.

(7) Key, B.; Bhattacharyya, R.; Morcrette, M.; Seznec, V.; Tarascon, J.-M.; Grey, C. P. *J. Am. Chem. Soc.* 2009, *131*,

(8) Grey, C. P.; Goward, G. R. *Solid State Nucl. Magn. Reson.* **2012**, *42*, 1.

(9) Yamakawa, N.; Jiang, M.; Key, B.; Grey, C. P. *J. Am. Chem. Soc.* **2009**, *131*, 10525.

(10) Dambournet, D.; Chapman, K. W.; Chupas, P. J.; Gerald, R. E.; Penin, N.; Labrugere, C.; Demourgues, A.; Tressaud, A.; Amine, K. *J. Am. Chem. Soc.* **2011**, *133*, 13240.

(11) Wang, F.; Robert, R.; Chernova, N. A.; Pereira, N.; Omenya, F.; Badway, F.; Hua, X.; Ruotolo, M.; Zhang, R.; Wu, L.; Volkov, V.; Su, D.; Key, B.; Whittingham, M. S.; Grey, C. P.; Amatucci, G. G.; Zhu, Y.; Graetz, J. *J. Am. Chem. Soc.* **2011**, *133*, 18828.

(12) Shyam, B.; Chapman, K. W.; Balasubramanian, M.; Klingler, R. J.; Srajer, G.; Chupas, P. J. *Angew. Chem., Int. Ed. Engl.* **2012**, *51*, 4852.

(13) The coherent neutron scattering cross sections of O and F differ by only 5%, less than the ~11% difference in the X-ray scattering lengths: F = 4.017 barn cf. O = 4.232 barn, $^{16}O$ = 4.232 barn, $^{17}O$ = 4.2 barn, $^{18}O$ = 4.29 barn.

(14) Dambournet, D.; Chapman, K. W.; Koudriachova, M. V.; Chupas, P. J.; Belharouak, I.; Amine, K. *Inorg. Chem.* **2011**, *50*, 5855.

(15) Mitome, M.; Kohiki, S.; Murakawa, Y.; Hori, K.; Kurashima, K.; Bando, Y. *Acta Crystallogr., Sect. B: Struct. Sci* **2004**, *60*, 698.

(16) Liao, P.; Li, J.; Dahn, J. R. *J. Electrochem. Soc.* **2010**, *157*, A355.

(17) Borkiewicz, O. J.; Shyam, B.; Wiaderek, K. M.; Kurtz, C.; Chupas, P. J.; Chapman, K. W. *J. Appl. Crystallogr.* **2012**, *45*, 1261.

(18) (a) Chupas, P. J.; Qiu, X.; Hanson, J. C.; Lee, P. L.; Grey, C. P.; Billinge, S. J. L. *J. Appl. Crystallogr.* **2003**, *36*, 1342. (b) Chupas, P. J.; Chapman, K. W.; Lee, P. L. *J. Appl. Crystallogr.* **2007**, *40*, 463.
(19) (a) Hammersley, A. P.; Svensson, S. O.; Hanfland, M.; Fitch, A. N.; Häusermann, D. *High Pressure Res.* **1996**, *14*, 235. (b) Hammersley, A. P. *ESRF Internal Report*, ESRF97HA02T; European Synchrotron Radiation Facility: Grenoble, France, 1997.
(20) Qiu, X.; Thompson, J. W.; Billinge, S. J. L. *J. Appl. Crystallogr.* **2004**, *37*, 678.
(21) Wojdyr, M. *J. Appl. Crystallogr.* **2010**, *43*, 1126.
(22) Farrow, C. L.; Juhás, P.; Liu, J. W.; Bryndin, D.; Božin, E. S.; Bloch, J.; Proffen, T.; Billinge, S. J. L. *J. Phys.: Condens. Matter* **2007**, *19*, 335219.
(23) Gross, U.; Rudiger, S.; Grimmer, A. R.; Kemnitz, E. *J. Fluorine Chem.* **2002**, *115*, 193.
(24) Chupas, P. J.; Chapman, K. W.; Jennings, G.; Lee, P. L.; Grey, C. P. *J. Am. Chem. Soc.* **2007**, *129*, 13822.
(25) Sougrati, M. T.; Chernova, N. A.; Omenya, F.; Pereira, N.; Amatucci, G. G.; Jumas, J. C. Personal communication; manuscript in preparation.
(26) Larcher, D.; Masquelier, C.; Bonnin, D.; Chabre, Y.; Masson, V.; Leriche, J. B.; Tarascon, J. M. *J. Electrochem. Soc.* **2003**, *150*, A133.
(27) Gmitter, A. J.; Badway, F.; Rangan, S.; Bartynski, R. A.; Halajko, A.; Pereira, N.; Amatucci, G. G. *J. Mater. Chem.* **2010**, *20*, 4149.
(28) Brese, N. E.; O'Keeffe, M. *Acta Crystallogr., Sect. B: Struct. Sci.* **1991**, *47*, 192.
(29) Adams, S. *Acta Crystallogr., Sect. B: Struct. Sci.* **2001**, *57*, 278.
(30) Grey, C. P.; Dupre, N. *Chem. Rev.* **2004**, *104*, 4493.
(31) Kim, J.; Nielsen, U. G.; Grey, C. P. *J. Am. Chem. Soc.* **2008**, *130*, 1285.
(32) Hess, A.; Kemnitz, E.; Lippitz, A.; Unger, W. E. S.; Menz, D. H. *J. Catal.* **1994**, *148*, 270.
(33) Doe, R. E.; Persson, K. A.; Meng, Y. S.; Ceder, G. *Chem. Mater.* **2008**, *20*, 5274.
(34) Chevrier, V. L.; Hautier, G.; Ong, S. P.; Doe, R. E.; Ceder, G. Submitted.